A flexible experimental setup for femtosecond time-resolved broad-band ellipsometry and magneto-optics

F. Boschini, H. Hedayat, C. Piovera, C. Dallera, A. Gupta, and E. Carpene

View Online   Export Citation   CrossMark

ARTICLES YOU MAY BE INTERESTED IN

A flexible experimental setup for femtosecond time-resolved broad-band ellipsometry and magneto-optics

F. Boschini,[1] H. Hedayat,[1] C. Piovera,[1] C. Dallera,[1] A. Gupta,[2] and E. Carpene[3,a]

[1]*Dipartimento di Fisica, Politecnico di Milano, p.zza Leonardo da Vinci 32, 20133 Milano, Italy*
[2]*Department of Chemistry, University of Alabama, Tuscaloosa, Alabama 35487, USA*
[3]*CNR-IFN, Dipartimento di Fisica, Politecnico di Milano, p.zza Leonardo da Vinci 32, 20133 Milano, Italy*

A versatile experimental setup for femtosecond time-resolved ellipsometry and magneto-optical Kerr effect measurements in the visible light range is described. The apparatus is based on the pump-probe technique and combines a broad-band probing beam with an intense near-infrared pump. According to Fresnel scattering matrix formalism, the analysis of the reflected beam at different polarization states of the incident probe light allows one to determine the diagonal and the off-diagonal elements of the dielectric tensor in the investigated sample. Moreover, the pump-probe method permits to study the dynamics of the dielectric response after a short and intense optical excitation. The performance of the experimental apparatus is tested on CrO_2 single crystals as a benchmark. © 2015 AIP Publishing LLC. [http://dx.doi.org/10.1063/1.4906756]

I. INTRODUCTION

Transient reflectivity via pump-probe method is a powerful and widely used technique to investigate electronic and lattice dynamics in a large class of materials and compounds. The technique is suitable for metals as well as semiconductors or dielectric samples, and it is based on a femtosecond laser source: a short (tens of fs) and intense (up to several mJ/cm^2) pulse perturbs the system under investigation, while a subsequent weak pulse probes the effect of the photoexcitation after a given delay. Due to the short pulse duration and to the fact that only electrons directly interact with light, transient reflectivity portrays the electronic response of the material to an external electromagnetic stimulus. Coupling between electrons and other degrees of freedom, such as lattice or spins in magnetically ordered compounds, can be inferred indirectly from the evolution of the reflected probe beam. By assuming linear response of a material to an electromagnetic wave, the effect of the pump pulse is to induce intraband and interband optical transitions that can transiently modify the dielectric properties of the sample and consequently its reflectivity. From the latter, the photo-induced modification to the dielectric tensor ε, or equivalently the conductivity tensor σ, can be deduced.[1,2]

Time-resolved ellipsometry with picosecond resolution dates back to the 1970s. Auston and Shank[3] exploited the pump-probe method and measured the change in the probe ellipticity to determine the evolution of the plasma density in germanium after an intense optical excitation. A different approach, where picosecond time-resolution could be achieved employing a fast detection technique (such as streak cameras), was proposed by Jellison and Lowndes in the 1980s.[4] The method allows to extrapolate the complex Fresnel coefficients (r_{ss} and r_{pp}) using a polarizer-compensator-sample-analyzer (PCSA) scheme. Simultaneous measurements of reflection and transmittance in pump-probe configuration have been used by Bergen *et al.*[5] to determine the evolution of the refractive index and absorption coefficient of silicon in a wide wavelength range (800 nm–1600 nm) with tens of picosecond time-resolution. In the 1990s, thanks to the development of commercial femtosecond laser sources, the pump-probe method became the most straightforward scheme to achieve unprecedented sub-picosecond time resolution. In 1994, Frenkel[6] developed a femtosecond reflectance ellipsometer to determine the change of the complex refractive index in optically thick samples. More recently, the ultrafast ellipsometric technique has been refined with various detection schemes in order to extrapolate real and imaginary parts of the dielectric tensor ε (Ref. 7) or the nonlinear susceptibility tensor χ.[8]

In cubic non-magnetic systems, ε reduces to a (complex) constant. Thus, two independent measurements are sufficient to fully characterize its real and imaginary parts. The common approach is to analyze the reflected and transmitted light intensities,[9–15] which implies the use of optically thin films on transparent substrates. The drawback of this method is that multiple reflections at the film interfaces (air-film and film-substrate) must be carefully accounted for. An alternative approach is to use optically thick samples (where light transmission is negligible) and exploit the polarization dependence of the reflected beam to determine the dielectric constant. The advantage of this procedure is to avoid any complication due to multiple reflections since only one discontinuity (the air-sample interface) reflects the laser beam. This is the approach we exploited.

When dealing with more complex crystal structures (non-cubic and/or in the presence of ferromagnetic order), the tensorial nature of ε must be considered, and for each additional tensor element (that is a complex number), two more measurements are needed in order to thoroughly determine the dielectric properties of the material.

a)Electronic address: ettore.carpene@polimi.it

In this work, we present a versatile experimental setup for femtosecond, time-resolved, broad-band ellipsometry, and magneto-optical measurements: the capabilities of the apparatus are tested on a tetragonal ferromagnetic system (CrO_2) where the three nontrivial (complex) elements of the dielectric tensor have been determined. The apparatus is based on an amplified Ti:Sapphire laser: the pump beam is a near infrared (IR) pulse (800 nm wavelength, 60 fs duration), while the probe beam is a broadband visible pulse (440-720 nm) with largely configurable polarization state. Section II of this article describes the laser source and the main features of the setup. Section III illustrates the capabilities of the system using a single crystalline CrO_2 sample as a benchmark. The Appendix reports the detailed description of the mathematical formalism used to extract the elements of the dielectric tensor from the experimental measurements.

II. EXPERIMENTAL SETUP

The light beam is provided by an amplified Ti:Sapphire laser (Coherent), working at repetition rate of 1 kHz and producing s-polarized, 60 fs pulses centered at 800 nm (1.55 eV), with average power of 1.5 W. Referring to Fig. 1, the infrared laser beam is split in two portions by a beam splitter (BS). The transmitted part enters a motorized delay stage and serves as pump; the reflected part passes through a band-pass filter (DF) centered at 810 ± 10 nm: it lengthens the IR pulse (centered at 800 nm) to roughly 100 fs in order to increase the stability of the subsequent non-linear optical process that creates the broadband pulse. After filtering, the probe power is about 0.5 mW, and it is focused by a lens (focal = 75 mm) inside a 1 mm thick sapphire plate generating the supercontinuum (SC, a broadband pulse in the visible spectral region ranging from 440 nm to 720 nm wavelength, see inset of Fig. 1).[16] The SC is collimated by a spherical mirror (focal = 75 mm), filtered to remove residual IR, and then focused by a spherical mirror (focal = 250 mm) on the sample at an incident angle

of 45° with respect to the surface normal. The choice of this specific incident angle is motivated in the Appendix. The polarization state of the SC beam is identical to the polarization of the generating IR pulse (s-pol), as verified with a polarizer. Before reaching the sample, the probe beam passes through a broadband quarter-waveplate changing its polarization state to circular. In some specific cases (discussed below), the quarter waveplate is replaced by a half-waveplate in order to rotate the s-polarization of 45° or 90° (p-pol). After reflection from the sample, the SC is collimated by a lens (focal 150 mm) and then passes through a polarizer (labeled "analyzer" in Fig. 1) used to select the desired polarization projection. Past the analyzer, a broadband half-waveplate rotates the polarization to s state (the reason will be illustrated in the following), and the probe beam is guided to the spectrometer (Princeton Instruments Acton Series, focal length of 300 mm, aperture f/3.9). The dispersion element of the spectrometer is a grating with 300 grooves/mm, and the spectra are collected by a CCD camera (Princeton Instruments Pixis, 1340×100 pixels) triggered to the laser beam (1 kHz) and configured to a readout time of about 0.8 ms. Rotating the probe polarization to s state after the analyzer is fundamental for ellipsometry measurements. The use of circularly polarized incident light allows us to select any polarization projection after reflection by the sample. In particular, we choose s-pol, p-pol, and 45°-pol projections since comparing the intensities of the reflected beam at these three polarization states, we can deduce the elements of the dielectric tensor. However, all mirrors that guide the probe beam to the spectrometer/CCD camera might significantly modify its intensity depending on the polarization. Thus, immediately after the analyzer, a broadband half-waveplate turns the probe to s-pol so that the beam intensity is unaltered during propagation to the CCD camera. The "check polarizer" is placed in the probe path only for control purpose. It is oriented in p-pol position; once the desired polarization projection is selected by the analyzer, the half-waveplate is rotated until total beam extinction is observed at the CCD camera, then the check polarizer is removed. This procedure guarantees the correct orientation of
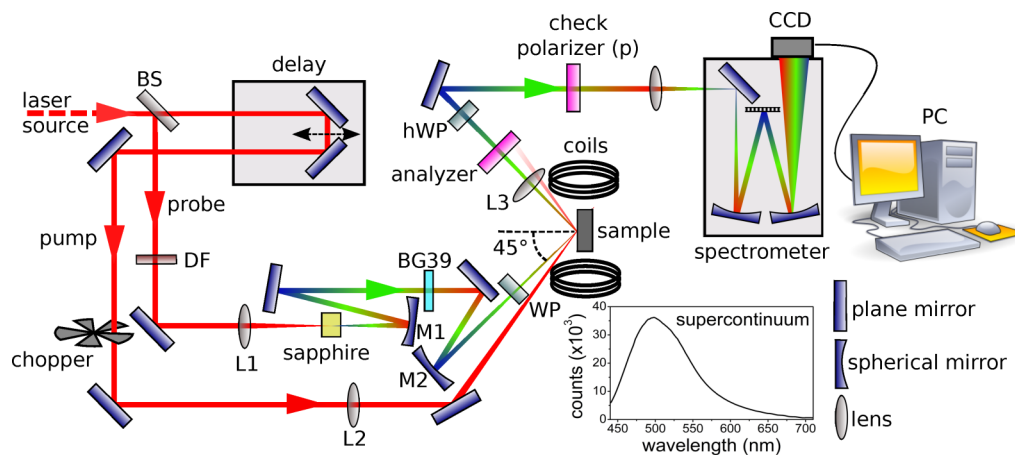

FIG. 1. Schematic view of the optical beamline dedicated to pump-probe ellipsometry. BS: beam splitter; DF: dichroic filter 810 ± 10 nm (it increases the supercontinuum stability); BG39: band-pass filter ($\approx$ 400–700 nm; it absorbs residual IR and transmits visible light); WP: (quarter- or half-) waveplate; hWP: half-waveplate; L1 lens (f = 75 mm) focuses the IR in the sapphire plate; M1 spherical mirror (f = 75 mm) collimates the SC; M2 spherical mirror (f = 250 mm) focuses the broadband probe on the sample; L3 lens (f = 150 mm) collimates the probe after reflection; and L2 lens (f = 500 mm) focuses the pump on the sample. The inset shows a typical SC spectrum.

the half-waveplate to achieve *s*-pol probe beam. Both analyzer and check polarizer are broadband Glan-Thompson prisms with extinction ratio $\sim10^{-5}$.

Time-resolved reflectivity data acquisition is performed in pump-on/pump-off modality: the pump beam is chopped at 500 Hz (half of the laser repetition rate) so that each subsequent probe beam will alternatively have its pump counterpart. For each pump-probe delay, a given number *n* of probe spectra are acquired by the CCD camera (typically 1000), the corresponding $n/2$ pump-on (S_{on}) and $n/2$ pump-off (S_{off}) spectra are averaged and the ratio $\delta_r = \langle S_{on}\rangle/\langle S_{off}\rangle - 1$ represents the normalized transient reflectivity $\Delta R/R$.

The same experimental setup can be used to perform time-resolved magneto-optical Kerr effect (TR-MOKE) analysis on ferromagnetic samples. In this case, the specimen is placed between Helmholtz coils, and the chopper on the pump beam is removed. The magnetic field between the coils is controlled by a pulsed current generator triggered to the laser source in order to produce opposite magnetic fields at the frequency of 500 Hz. Thus, the sample magnetization is reversed every millisecond and each subsequent laser pulse will detect opposite magnetization states. Similarly to the case of transient reflectivity, *n* probe spectra are acquired by the CCD camera, the corresponding $n/2$ spectra at positive magnetic field (S_+) and $n/2$ spectra at negative magnetic field (S_-) are averaged, then the ratio $\delta_m = \langle S_+\rangle/\langle S_-\rangle - 1$ is computed. Using the Jones scattering matrix formalism, it can be shown that δ_m is proportional to the Kerr rotation θ or Kerr ellipticity η, depending on the polarization of the incident light.[17] In particular, using circularly polarized light, we obtain $\langle S_+\rangle = R(1/2 + \eta)$ and $\langle S_-\rangle = R(1/2 - \eta)$ (*R* being the reflectivity), therefore $\delta_m \simeq 4\eta$, while using light linearly polarized at 45° (in this case, the quarter waveplate before the sample is replaced by a half-waveplate), we have $\langle S_+\rangle = R(1/2 + \theta)$ and $\langle S_-\rangle = R(1/2 - \theta)$, thus $\delta_m \simeq 4\theta$. The coils can be arranged in order to orient the magnetic field (and consequently the sample magnetization) along specific directions: (i) longitudinal, i.e., parallel to the light scattering plane and to the sample surface, (ii) transverse, i.e., normal to the light scattering plane, and (iii) polar, i.e., normal to the sample surface.

The use of broadband probe pulses presents an intrinsic synchronization problem with the pump pulse: as they travel through dispersive optical elements, each wavelength experiences different group velocities, reaching the sample at different times. This phenomenon (called "chirp") is clearly visible in the time-resolved reflectivity spectra shown in Fig. 2. The zero pump-probe delay varies as a function of the probe wavelength and, in particular (see Fig. 2(b)), it spans over $\Delta t \simeq 730$ fs for a band width $\Delta\lambda \simeq 210$ nm (from 485 nm to 695 nm). This effect is produced by the sapphire plate generating the SC, the filter (BG), and the waveplates. However, it is important to stress that time resolution is unaffected: even assuming linear chirp, we have $\Delta t/\Delta\lambda \simeq 4$ fs/nm, i.e., wavelengths 1 nm apart experience a mutual delay of 4 fs. The spectral resolution of our spectrometer is about 0.2 nm (the whole SC spectrum spanning roughly 280 nm is dispersed on the 1340 pixels of the CCD, corresponding to about 0.2 nm/pixel): therefore, the temporal chirp is shorter than 1 fs/pixel, that is, much better than our pulse duration. To increase the
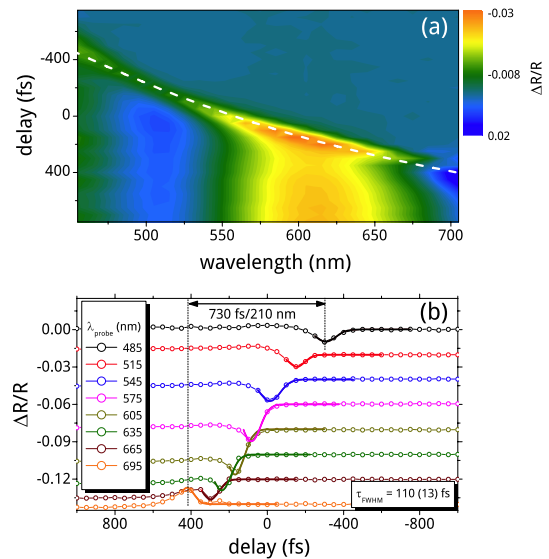

FIG. 2. (a) False color representation of time- and wavelength-resolved reflectivity in a 300 nm $CrO_2(100)$ film. The zero pump-probe delay varies continuously due to the chirp effect of the probe beam; (b) comparison among transient reflectivity for selected probe wavelengths: the zero delay spans over 730 fs for a bandwidth of 210 nm (from 485 nm to 695 nm). The sharp peaks in panel (b) (attributed to pump-induced, non-thermal electronic contribution, as suggested in Ref. 18) have been used to estimate the pump-probe cross-correlation obtaining a FWHM value of 110 ± 13 fs.

signal/noise ratio, contiguous pixels are merged in groups of 5 (i.e., ~5 fs/group). The time resolution of our setup has been evaluated directly from the transient reflectivity spectra: as shown in Fig. 2(b), CrO_2 displays a sharp peak at zero pump-probe delay (its temporal position shifts with the probe wavelength according to the chirp effect) that is attributed to the pump-induced, non-thermal electronic distribution.[18] Therefore, it should mimic the pump duration at least for negative delays (i.e., the peak formation). Neglecting the positive delay-side of the peak that is affected by relaxation processes and by the emergence of other electronic contributions, a gaussian fit provides the pump-probe cross-correlation. The fitting curves are shown in Fig. 2(b) as the solid lines and the resulting cross-correlation (FWHM) is $\tau_{FWHM} = 110 \pm 13$ fs with no significant dependence on the probe wavelength.

III. TESTS AND RESULTS

A. Static case

We have tested the capability of the experimental setup on $CrO_2(100)$ films with thickness ranging from 150 nm to 300 nm, epitaxially grown on $TiO_2(100)$ substrates by CVD[19] Chromium dioxide has tetragonal crystallographic structure (base axes $a = b = 4.41$ Å, $c = 2.91$ Å) and it is ferromagnetic below $T_C = 395$ K. Spins align along *c* axis that, in our samples, lies along the sample surface (in-plane magnetization). It is a half-metallic ferromagnet with 100% spin polarization at the Fermi level[20] and its electronic and optical properties have been thoroughly computed.[21–25] According to its crystallographic and magnetic structure, the (complex) dielectric

tensor of CrO_2 has the following form:

$$\boldsymbol{\varepsilon} = \boldsymbol{\varepsilon}' + i\boldsymbol{\varepsilon}'' = \begin{pmatrix} \varepsilon_{xx} & \varepsilon_{xy} & 0 \\ -\varepsilon_{xy} & \varepsilon_{xx} & 0 \\ 0 & 0 & \varepsilon_{zz} \end{pmatrix} \quad (1)$$

with a, b, c parallel to x, y, z, respectively. We point out that the off-diagonal element $\varepsilon_{xy} \ll \varepsilon_{xx}, \varepsilon_{zz}$. We will now focus on the diagonal elements of the dielectric tensor. The analysis of the off-diagonal component will be discussed in Sec. III C.

The static values of ε_{xx} and ε_{zz} in the spectral range of the probe beam (440-720 nm) are deduced by measuring the reflected light intensity with three different polarization projections (s, p, and 45°) in two different geometries: longitudinal, i.e., c axis parallel to the light scattering plane, and transverse, i.e., c axis normal to the scattering plane (the detailed procedure is described in the Appendix). Figs. 3(a) and 3(b) report the measurements. The insets show the intensity spectra I_s, I_p, I_{45} of the reflected probe beams for the three polarization projections, while the graphs represent the ratios I_p/I_s and I_{45}/I_s. From these ratios, through a numerical procedure, the diagonal elements of the dielectric tensor are extrapolated. Fig. 3(c) shows real (black lines) and imaginary (red lines) parts of ε_{xx} (solid lines) and ε_{zz} (dashed lines) in the probe
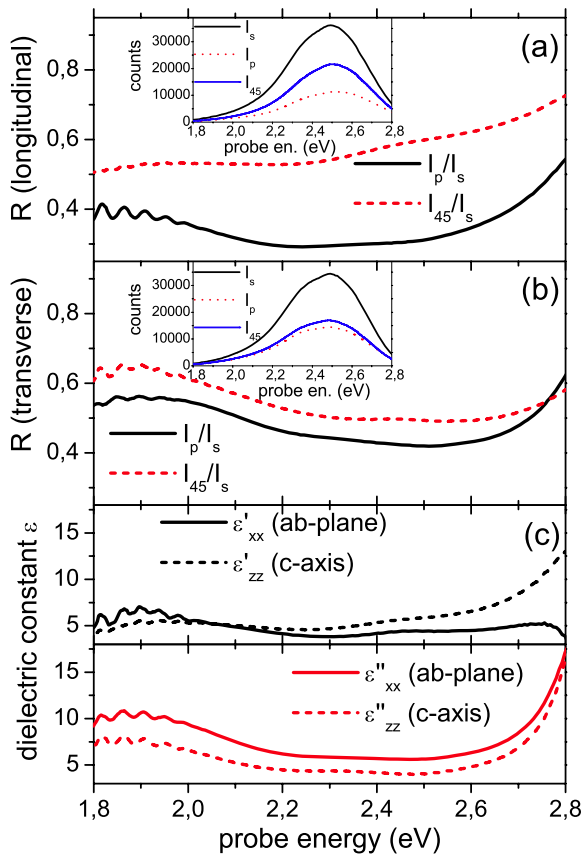

FIG. 3. Intensity ratios I_p/I_s and I_{45}/I_s of the reflected spectra of CrO_2 for different polarization projections (s, p, and 45°) as a function of the probe energy in (a) longitudinal configuration of the sample, i.e., c-axis parallel to the light propagation plane, and (b) transverse configuration, i.e., c-axis normal to the propagation plane (see also Fig. 8). The insets show the reflected spectra. (c) Diagonal elements of the dielectric tensor (real and imaginary parts) extrapolated from the intensity ratios.

spectral range. The two diagonal elements differ from each other due to the birefringence of CrO_2.[26]

B. Dynamic case

The pump-probe technique allows us to investigate the modification of the dielectric tensor induced by a short and intense optical excitation. Since four unknown quantities must be determined in CrO_2 (real and imaginary parts of ε_{xx} and ε_{zz}), four independent measurements are necessary. Thus, transverse and longitudinal transient reflectivities for s-pol and 45°-pol projections are acquired. Fig. 4 reports the room temperature s-pol transient reflectivity in transverse (a) and longitudinal (b) geometries as a function of the probe wavelength and the pump-probe delay (the 45°-pol data are qualitatively similar and they are not reported here for brevity). Figs. 4(c) and 4(d) (solid lines) show the temporal evolution of $\Delta R/R$ for two selected probe wavelengths (540 nm and 640 nm). It is interesting to observe how the transient signal changes sign depending on the geometry of the experiment. This is a clear signature of the birefringent behavior of CrO_2: as reported in the Appendix (Eqs. (A21)–(A23)), s-pol longitudinal and transverse measurements are sensitive to ε_{xx} and ε_{zz}, respectively. An interesting feature is the gradual increase of the transient signal for pump-probe delay up to 50 ps. It is particularly evident in the transverse case (Fig. 4(c)), corresponding to ε_{zz}, i.e., along the c crystallographic axis parallel to the magnetization. This effect disappears if the measurement is performed above the Curie temperature (T_C = 395 K) of CrO_2. Dashed lines in panels (c) and (d) represent the transient reflectivity at the reported wavelengths and under the same geometrical conditions corresponding to the solid lines, but holding the sample at 420 K. The increase of transient reflectivity at large pump-probe delay has been observed in other ferromagnetic half-metals and it is attributed to spin-lattice relaxation.[27,28]

The extrapolation of $\boldsymbol{\varepsilon}$ from reflectivity measurements provides the link between optical properties and electronic structure of a material. We recall that $\boldsymbol{\varepsilon}$ relates to the conductivity tensor $\boldsymbol{\sigma} = \boldsymbol{\sigma}' + i\boldsymbol{\sigma}''$ as

$$\boldsymbol{\varepsilon} = \boldsymbol{\varepsilon}'(\omega) + i\boldsymbol{\varepsilon}''(\omega) = \boldsymbol{I} + \frac{4\pi i}{\omega}[\boldsymbol{\sigma}'(\omega) + i\boldsymbol{\sigma}''(\omega)] \quad (2)$$

with ω being the frequency of the probe electric field (thus, $\hbar\omega$ is the probe photon energy). Notice how the real part $\boldsymbol{\sigma}'$ determines the imaginary part $\boldsymbol{\varepsilon}''$, and vice-versa. The diagonal elements of $\boldsymbol{\sigma}'$ (and thus of $\boldsymbol{\varepsilon}''$) describe the absorption of electromagnetic waves, which relates to the joint density of states (JDOS) of the material, a quantity that can be deduced from electronic band structure calculations.

Restricting to diagonal elements only, from Eq. (2), it can be easily deduced that the relative variation of ε'' is identical to the relative change of σ',

$$\frac{\Delta\varepsilon''}{\varepsilon''} = \frac{4\pi\Delta\sigma'}{\omega} / \frac{4\pi\sigma'}{\omega} = \frac{\Delta\sigma'}{\sigma'}. \quad (3)$$

Fig. 5(a) reports $\Delta\varepsilon''_{xx}/\varepsilon''_{xx}$ and $\Delta\varepsilon''_{zz}/\varepsilon''_{zz}$ as a function of the probe photon energy at two selected pump-probe delays: 3 ps (dashed line) and 100 ps (solid line). The relative increase of
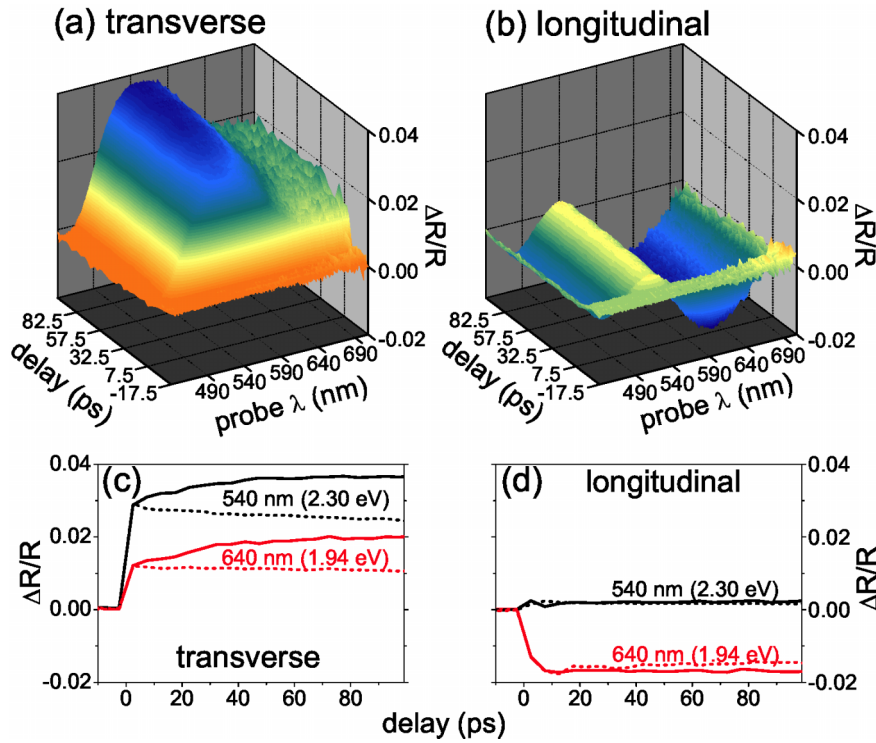
(a) transverse

(b) longitudinal

FIG. 4. Room temperature, time- and spectrum-resolved transient reflectivity $\Delta R_s/R_S$ for (a) transverse and (b) longitudinal configuration of CrO$_2$. The lower graphs show the corresponding transient reflectivities for two selected probe wavelengths (540 nm and 640 nm) for clarity. Solid lines are room temperature measurements, dashed lines are measurements at 420 K (i.e., above the Curie point). The high temperature data have been properly rescaled for comparison purpose.
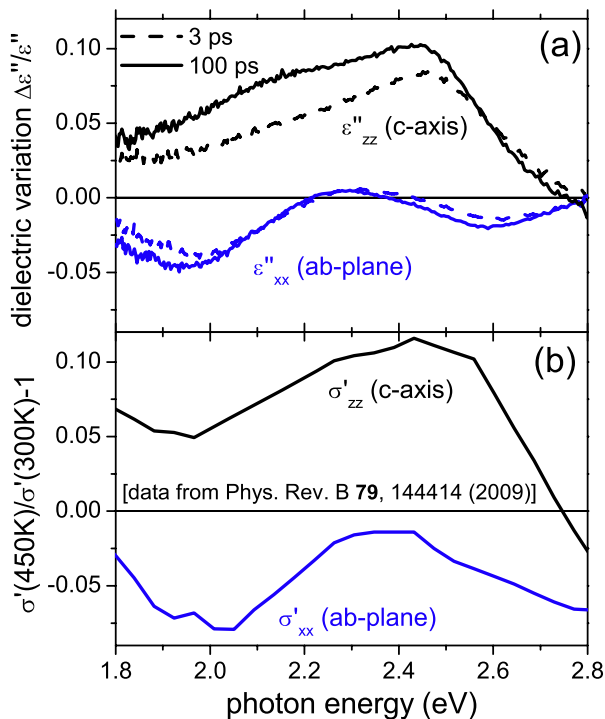

FIG. 5. (a) Pump-induced variation of the imaginary parts of the diagonal elements $\Delta\varepsilon''/\varepsilon''$ along the c-axis (top) and on the ab-plane (bottom) of CrO$_2$, as extrapolated from the transient reflectivity data; dashed line corresponds to pump-probe delay of 3 ps, solid line to 100 ps delay. (b) Optical conductivity ratio [$\sigma'(450\,\text{K})/\sigma'(300\,\text{K}) - 1$] as extrapolated from Ref. 29 showing the thermal variation of σ' along the c-axis (top) and on the ab-plane (bottom) of CrO$_2$.

the transient signals at large delay is particularly evident along the c-axis and is ascribed to spin-lattice relaxation, as already argued from the reflectivity measurements. Fig. 5(b) shows the relative thermal variation of the optical conductivity along the c-axis (σ'_{zz}) and on the ab-plane (σ'_{xx}) in the same spectral range. These data are extrapolated from static ellipsometric measurements of Ref. 29 and, in particular, they represent the ratio

$$\frac{\sigma'_{\alpha\alpha}(450\,\text{K}) - \sigma'_{\alpha\alpha}(300\,\text{K})}{\sigma'_{\alpha\alpha}(300\,\text{K})} = \frac{\sigma'_{\alpha\alpha}(450\,\text{K})}{\sigma'_{\alpha\alpha}(300\,\text{K})} - 1 \qquad (4)$$

(with $\alpha = x, z$) which depicts the thermal dependence of σ'_{xx} and σ'_{zz}. Both qualitative and quantitative agreements between our time-resolved data and the temperature-dependent data of Ref. 29 are very good. These measurements indicate that the variation of the optical conductivity induced by an ultrashort laser pulse is dominated by thermal effects after a few picoseconds. Keeping in mind that thermal equilibrium between electrons and lattice sets in within a picosecond past the pump pulse,[18] this conclusion is perfectly reasonable. Referring to Fig. 5(a), our time-resolved analysis reveals the strong spin-lattice effect along the c-axis, i.e., parallel to the magnetization direction. The microscopic origin of this phenomenon is beyond the scope of this report, but it has been observed with pump-probe reflectivity measurements on other ferromagnetic half-metals and its explanation is still a matter of debate.[30] However, our experimental method to derive the transient optical conductivity provides an useful tool to test or endorse theoretical models.

C. Magneto-optics

We will now focus on the analysis of the ferromagnetic case. As explained in Sec. II, using linearly and circularly polarized probe beams, we have access to Kerr rotation θ and Kerr ellipticity η, the real and imaginary parts, respectively, of the complex Kerr angle Θ. The TR-MOKE measurements have been performed in longitudinal configuration analyzing the p-pol projection of the reflected light. It can be shown that the Kerr angle is proportional to the off-diagonal elements ε_{xy} of the dielectric tensor, that is, the physical quantity directly connected to ferromagnetic order.[17] In particular,

$$\Theta_p = \theta_p + i\eta_p = f_p \times \varepsilon_{xy}. \qquad (5)$$

In the specific case of CrO_2, the complex quantity f_p is a function of the diagonal elements ε_{xx} and ε_{zz} of the dielectric tensor (the explicit formula is reported in the Appendix). Eq. (5) reveals a criticality that manifests itself in time-resolved experiments: optical excitations affect the diagonal terms of the dielectric tensor, as demonstrated in Sec. III B, but can modify the off-diagonal element ε_{xy} (i.e., the spin order) as well. Restricting TR-MOKE analysis to rotation or ellipticity alone does not clarify whether the observed transient magneto-optics effects are due to optically induced variation of ε_{xy} or just artifact deriving from the temporal evolution of ε_{xx} and ε_{zz}. In order to achieve the genuine magnetic signal, it is essential to isolate the variation of ε_{xy} from the other terms. We have recently demonstrated that such separation can be successfully performed with time-resolved experiment at 800 nm pump and probe wavelengths.[17] Here, we extend previous results to the broadband probe case. Fig. 6(a) reports the static longitudinal Kerr rotation (solid line) and ellipticity (dashed line) as a function of the probe photon energy. As shown in Sec. III A, also ε_{xx} and ε_{zz} have been deduced in the
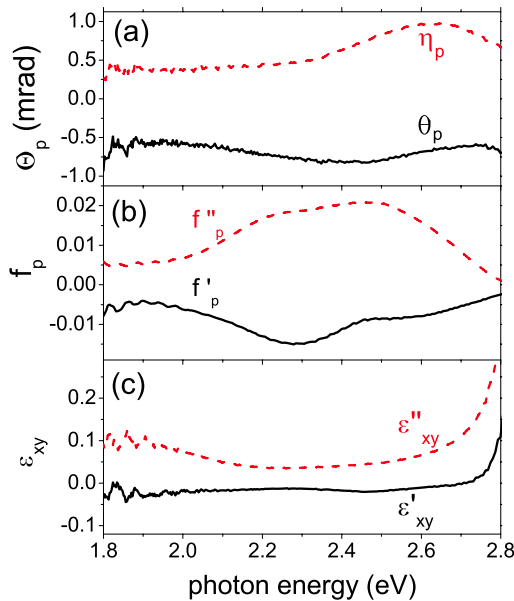
FIG. 6. Static measurements in the probe spectral range of (a) longitudinal Kerr rotation (solid) and ellipticity (dashed) of CrO_2 (p-pol projection); (b) real (solid) and imaginary (dashed) parts of the complex function f_P extrapolated from the diagonal elements of the dielectric tensor (see text for explanation); and (c) real (solid) and imaginary (dashed) parts of the off-diagonal tensor element of CrO_2.
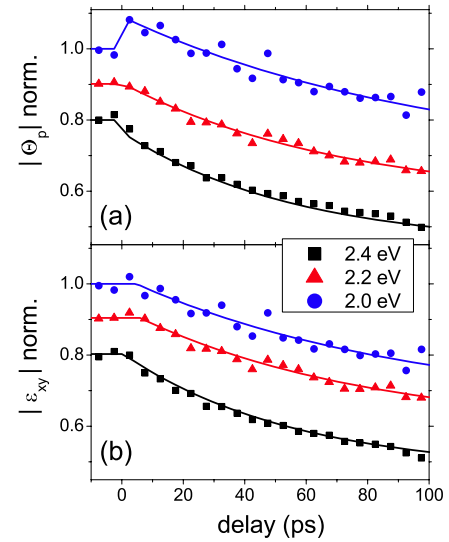
FIG. 7. Time-resolved evolution of the normalized moduli of (a) the Kerr angle $|\Theta_P|$ and (b) the off-diagonal element $|\varepsilon_{xy}|$ of the dielectric tensor of CrO_2 for three selected probe photon energies (2 eV, 2.2 eV, and 2.4 eV). The curves are vertically shifted for clarity. The prompt increase of $|\Theta_P|$ at zero pump-probe delay for 2 eV probe beam is due to nonmagnetic effects.

same spectral range (see Fig. 3(c)). According to the formulas reported in the Appendix, the term f_p can be explicitly written as a function of ε_{xx} and ε_{zz}, which allows us to determine its real and imaginary parts, as reported in Fig. 6(b). Therefore, using Eq. (5), the real and imaginary parts of the off-diagonal element ε_{xy} can be extracted. The result is shown in Fig. 6(c). The experimental data shown in Figs. 3(c) and 6(c) provide the complete dielectric characterization of CrO_2 in the probe spectral range (1.8-2.8 eV).

The temporal evolution of ε_{xy} after the pump excitation can be obtained from TR-MOKE measurements (i.e., the evolution of the complex Kerr angle) and transient reflectivity data that provide the time evolution of f_p. According to Onsager's relations, it is customary to assume $|\varepsilon_{xy}| \propto M$. Therefore, without loss on generality, in the following, we will consider only the moduli of complex quantities. Due to the half-metallic character that inhibits spin-flip, optically induced demagnetization occurs on a 100 ps timescale.[18,31] The comparison between time-resolved, normalized $|\Theta_P|$ and $|\varepsilon_{xy}|$ is reported in Fig. 7 for three selected probe photon energies (2 eV, 2.2 eV, and 2.4 eV). The presence of nonmagnetic artifacts due to transient effects in the function f_p becomes particularly evident: at probe photon energy of 2 eV, the modulus of the Kerr angle shows a prompt increase at zero pump-probe delay (blue curve in Fig. 7(a)), which would suggest a rapid enhancement of the magnetic order upon pump arrival. However, such effect is not observed in the modulus of $|\varepsilon_{xy}|$ (blue curve in Fig. 7(b)). Thanks to our detailed ellipsometric analysis, the genuine spin dynamics (represented by $|\varepsilon_{xy}|$) can be obtained.

IV. CONCLUSIONS

In this work, we have presented the performances of the novel experimental setup dedicated to femtosecond time-resolved ellipsometry and magneto-optical spectroscopy. The

versatility of the light source and, in particular, the large freedom in the choice of spectral range and polarization state of the probing beam allow us to characterize the dielectric properties of the investigated material. This flexibility grants the possibility to access the pump-induced evolution of the dielectric tensor in the visible-spectra range (1.8-2.8 eV) as well as the genuine spin dynamics in ferromagnetic compounds.

ACKNOWLEDGMENTS

APPENDIX: JONES MATRIX FORMALISM

The linear response of a material to an electromagnetic wave is determined by the first-order dielectric tensor ε (a 3×3 matrix). In the proper axes frame, nonferromagnetic materials with orthorhombic symmetry have only diagonal elements in the dielectric tensor ($\varepsilon_{\alpha\beta} = 0$ if $\alpha \neq \beta$). When ferromagnetic order is present, also off-diagonal elements appear,[1]

$$\varepsilon = \begin{pmatrix} \varepsilon_{xx} & \varepsilon_{xy} & 0 \\ -\varepsilon_{xy} & \varepsilon_{yy} & 0 \\ 0 & 0 & \varepsilon_{zz} \end{pmatrix}, \tag{A1}$$

where ε_{xx}, ε_{yy}, and ε_{zz} are the permittivities along the a, b, and c crystallographic axes, respectively, while ε_{xy} is due to the presence of magnetic order along the c axis. Here, we will first illustrate in detail the simple case of non-magnetic cubic symmetry ($\varepsilon_{xx} = \varepsilon_{yy} = \varepsilon_{zz}$, $\varepsilon_{xy} = 0$).

The complex dielectric constant ε_{xx} is extracted using the Jones matrix formalism. According to the conventional notation, the 2-dimensional vectors $p = (1, 0)$, $s = (0, 1)$, and $c = (i, 1)/\sqrt{2}$ represent p-polarized, s-polarized, and circular polarized light, respectively. After reflection from the sample, the intensity and polarization state of light are determined by the 2×2 scattering matrix $\mathbb{S}$,[32–34]

$$\mathbb{S} = \begin{pmatrix} r_{pp} & r_{ps} \\ r_{sp} & r_{ss} \end{pmatrix}. \tag{A2}$$

The four matrix elements depend on the terms of the dielectric tensor of the material and on the light incidence angle θ (45° in our setup). The off-diagonal elements are typically two orders of magnitude smaller than the diagonal ones and they are proportional to ε_{xy}. Thus, in non-magnetic materials, they are identically zero. If the probe incidence angle is 45°, the diagonal elements of the scattering matrix reduce to the following expressions:

$$r_{pp} = \frac{\varepsilon_{xx} - \sqrt{2\varepsilon_{xx} - 1}}{\varepsilon_{xx} + \sqrt{2\varepsilon_{xx} - 1}}, \tag{A3}$$

$$r_{ss} = \frac{1 - \sqrt{2\varepsilon_{xx} - 1}}{1 + \sqrt{2\varepsilon_{xx} - 1}}. \tag{A4}$$

It should be noticed that at this incidence angle, $r_{pp} = r_{ss}^2$. The quantity ε_{xx} can be deduced using circularly polarized incident light and measuring three different polarization projec-

tions of the spectra reflected by the sample. The projection is selected by the analyzer (whose Jones matrix is $\mathbb{P}$) placed after the sample, and the reflected beam is described by the vector $\mathbb{P} \cdot \mathbb{S} \cdot c$, with

$$\mathbb{P}_s = \begin{pmatrix} 0 & 0 \\ 0 & 1 \end{pmatrix}, \mathbb{P}_p = \begin{pmatrix} 1 & 0 \\ 0 & 0 \end{pmatrix}, \mathbb{P}_{45} = \frac{1}{2}\begin{pmatrix} 1 & 1 \\ 1 & 1 \end{pmatrix} \tag{A5}$$

being the Jones matrix of the s, p, and 45° polarization projections, respectively. The corresponding (normalized) beam intensities after the analyzer become

$$\frac{I_s}{I_0} = |\mathbb{P}_s \cdot \mathbb{S} \cdot c|^2 = \frac{|r_{ss}|^2}{2} = \frac{R_s}{2}, \tag{A6}$$

$$\frac{I_p}{I_0} = |\mathbb{P}_p \cdot \mathbb{S} \cdot c|^2 = \frac{|r_{pp}|^2}{2} = \frac{R_p}{2}, \tag{A7}$$

$$\frac{I_{45}}{I_0} = |\mathbb{P}_{45} \cdot \mathbb{S} \cdot c|^2 = \frac{|r_{pp}|^2 + |r_{ss}|^2 - 2\Im(r_{pp}r_{ss}^*)}{4} \tag{A8}$$

$$= \frac{R_p + R_s - 2\Im(r_{pp}r_{ss}^*)}{4}, \tag{A9}$$

where I_0 in the intensity of the incoming probe beam. By taking the ratios

$$I_p/I_s = R_p/R_s = |r_{pp}|^2/|r_{ss}|^2, \tag{A10}$$

$$I_{45}/I_s = \frac{I_p/I_s + 1 - 2\Im(r_{pp}/r_{ss})}{2}, \tag{A11}$$

we obtain two coupled equations (independent of I_0) that, through Eqs. (A3) and (A4), can be numerically solved to obtain the two unknown quantities, i.e., real and imaginary parts of ε_{xx}. Thus, measuring the reflected probe spectra at three different polarization projections (p, s, 45°), we can derive ε_{xx}.

Once the static value of ε_{xx} is known, the dynamics of the dielectric tensor, as induced by optical pumping, can be deduced from the transient reflectivity δ. In particular, two polarization projections are needed (s and 45°). The two transient reflectivities are

$$\delta_s = \Delta R_s/R_s = R_s^t/R_s - 1, \tag{A12}$$

$$\delta_{45} = \Delta R_{45}/R_{45} = R_{45}^t/R_{45} - 1, \tag{A13}$$

where R_s and R_{45} are the static reflectivities for the two polarization states, while R_s^t and R_{45}^t are the corresponding quantities at a given delay t after the pump arrival. According to the previous relations, we obtain

$$R_s^t = (1 + \delta_s)R_s, \tag{A14}$$

$$R_{45}^t = (1 + \delta_{45})R_{45}, \tag{A15}$$

where the following equalities hold:

$$R_s = |r_{ss}|^2, \tag{A16}$$

$$R_s^t = |r_{ss}^t|^2, \tag{A17}$$

$$R_{45} = (|r_{pp}|^2 + |r_{ss}|^2 - 2\Im(r_{pp}r_{ss}^*)), \tag{A18}$$

$$R_{45}^t = (|r_{pp}^t|^2 + |r_{ss}^t|^2 - 2\Im(r_{pp}^t r_{ss}^{t*})). \tag{A19}$$

Eqs. (A14) and (A15) represent two coupled equations that can be solved numerically through Eqs. (A3) and (A4) to access the real and imaginary part of ε_{xx}^t, i.e., the evolution of the permittivity after the optical excitation.
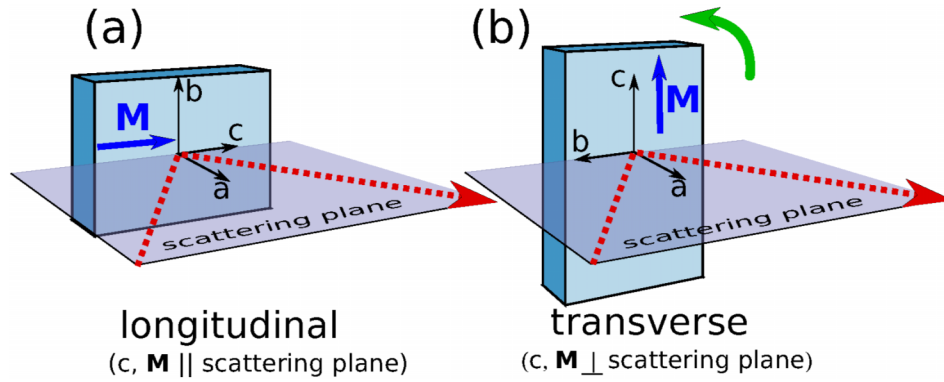
FIG. 8. (a) Longitudinal sample geometry: the c-axis of CrO_2 lies on the light scattering plane. (b) Transverse geometry: the c-axis is normal to the light scattering plane. The two geometries differ by a 90° rotation about the surface normal. In the ferromagnetic phase, the magnetization M points along the c-axis.

The previous discussion applies to samples with cubic symmetry, but it can be adapted to more complex ones. Particularly interesting is the case of CrO_2, i.e., a ferromagnetic oxide with tetragonal structure (i.e., two different diagonal elements are expected), where the c-axis is also the spin direction. Thus, imposing $\varepsilon_{xx} = \varepsilon_{yy}$ in Eq. (A1), we obtain the dielectric tensor of CrO_2. In the following, two representative geometries are considered: longitudinal (Fig. 8(a)), with the c-axis lying in the light scattering plane, and transverse (Fig. 8(b)), with the c-axis normal to the light incidence plane (we can switch from one geometry to the other rotating the sample by 90° about the a-axis). As assumed earlier, if the light incidence angle is 45°, the diagonal elements of the scattering matrix (Eq. (A2)) reduce to the following expressions, depending on the sample geometry:

$$r_{pp}(lon) = \frac{\sqrt{\varepsilon_{xx}\varepsilon_{zz}} - \sqrt{2\varepsilon_{xx}-1}}{\sqrt{\varepsilon_{xx}\varepsilon_{zz}} + \sqrt{2\varepsilon_{xx}-1}}, \tag{A20}$$

$$r_{ss}(lon) = \frac{1 - \sqrt{2\varepsilon_{xx}-1}}{1 + \sqrt{2\varepsilon_{xx}-1}}, \tag{A21}$$

$$r_{pp}(tra) = \frac{\varepsilon_{xx} - \sqrt{2\varepsilon_{xx}-1}}{\varepsilon_{xx} + \sqrt{2\varepsilon_{xx}-1}}, \tag{A22}$$

$$r_{ss}(tra) = \frac{1 - \sqrt{2\varepsilon_{zz}-1}}{1 + \sqrt{2\varepsilon_{zz}-1}}. \tag{A23}$$

In a tetragonal (non-magnetic) material, there are 4 unknown dielectric quantities (real and imaginary parts of ε_{xx} and ε_{zz}). Using Eqs. (A10), (A11), (A14), and (A15) for both geometries (longitudinal and transverse), we obtain 4 coupled equations that lead to the static and time-resolved values of ε_{xx} and ε_{zz}.

For completeness, we conclude describing the MOKE measurements. The complex Kerr angle $\Theta = \theta + i\eta$ is proportional to the off-diagonal elements of the dielectric tensor, i.e., $\Theta = f \times \varepsilon_{xy}$: ε_{xy} is the physical quantity carrying the magnetic information, while f depends on the diagonal elements of the dielectric tensor. In particular, for longitudinal configuration (M parallel to the light incidence plane and to the sample surface) and depending on the projection selected

by the analyzer (s or p), we have

$$\Theta_{s,p} = \theta_{s,p} + i\eta_{s,p} \tag{A24}$$

$$= -r_{ps}/r_{ss,pp} \tag{A25}$$

$$= \frac{2\sqrt{2\varepsilon_{zz}}}{\beta(\beta \pm 1)(\beta \mp \sqrt{\varepsilon_{xx}\varepsilon_{zz}})(\sqrt{\varepsilon_{xx}} + \sqrt{\varepsilon_{zz}})} \times \varepsilon_{xy} \tag{A26}$$

$$= f_{s,p} \times \varepsilon_{xy} \tag{A27}$$

with $\beta = \sqrt{2\varepsilon_{xx}-1}$ (the upper sign refers to p-pol, the lower sign to s-pol). Notice that if $\varepsilon_{xx} = \varepsilon_{zz}$ (cubic symmetry), the previous formulas simplify to

$$\Theta_{s,p} = \frac{\sqrt{2}}{\beta(\beta \pm 1)(\beta \mp \varepsilon_{xx})} \times \varepsilon_{xy}. \tag{A28}$$

In Eqs. (A26)–(A28), we have assumed 45° incidence angle of the probe. Once the diagonal elements ε_{xx} and ε_{zz} are known, the complex function f can be fully determined. Thus, the experimental measurements of θ and η allow one to numerically obtain real and imaginary parts of ε_{xy}.

[1]V. Antonov, B. Harmon, and A. Yeresko, *Electronic Structure and Magneto-Optical Properties of Solids* (Kluwer, New York, 2004).
[2]M. Dressel and G. Grüner, *Electrodynamics of Solids, Optical Properties of Electrons in Matter* (Cambridge University Press, 2003).
[3]D. H. Auston and C. V. Shank, Phys. Rev. Lett. **32**, 1120 (1974).
[4]G. E. Jellison and D. H. Lowndes, Appl. Opt. **24**, 2948 (1985).
[5]H. Bergen, V. Brückner, L. Leine, and M. Supianek, Appl. Phys. A **43**, 97 (1987).
[6]M. Y. Frenkel, Opt. Lett. **19**, 1252 (1994).
[7]H. Yoneda, H. Morikami, K. Ueda, and R. M. More, Phys. Rev. Lett. **91**, 075004 (2003).
[8]V. V. Kruglyak, R. J. Hicken, M. Ali, B. J. Hickey, A. T. G. Pyn, and B. K. Tanner, Phys. Rev. B **71**, 233104 (2005).
[9]C.-K. Sun, F. Vallée, L. H. Acioli, E. P. Ippen, and J. G. Fujimoto, Phys. Rev. B **50**, 15337 (1994).
[10]N. D. Fatti, C. Voisin, M. Achermann, S. Tzortzakis, D. Christofilos, and F. Vallée, Phys. Rev. B **61**, 16956 (2000).
[11]J. Demsar, R. D. Averitt, K. H. Ahn, M. J. Graf, S. A. Trugman, V. V. Kabanov, J. L. Sarrao, and A. J. Taylor, Phys. Rev. Lett. **91**, 027401 (2003).
[12]M. Bonn, D. N. Denzler, S. Funk, M. Wolf, S.-S. Wellershoff, and J. Hohlfeld, Phys. Rev. B **61**, 1101 (2000).
[13]E. Carpene, Phys. Rev. B **74**, 024301 (2006).
[14]G. D. Valle, M. Conforti, S. Longhi, G. Cerullo, and D. Brida, Phys. Rev. B **86**, 155139 (2012).
[15]P. B. Allen, Phys. Rev. Lett. **59**, 1460 (1987).
[16]G. Cerullo and S. De Silvestri, Rev. Sci. Instrum. **74**, 1 (2003).
[17]E. Carpene, F. Boschini, H. Hedayat, C. Piovera, C. Dallera, E. Puppin, M. Mansurova, M. Münzenberg, X. Zhang, and A. Gupta, Phys. Rev. B **87**, 174437 (2013).

[18] Q. Zhang, A. V. Nurmikko, G. X. Miao, G. Xiao, and A. Gupta, Phys. Rev. B **74**, 064414 (2006).

[19] G. Miao, G. Xiao, and A. Gupta, Phys. Rev. B **71**, 094418 (2005).

[20] J. M. D. Coey and M. Venkatesan, J. Appl. Phys. **91**, 8345 (2002).

[21] S. P. Lewis, P. B. Allen, and T. Sasaki, Phys. Rev. B **55**, 10253 (1997).

[22] I. I. Mazin, D. J. Singh, and C. Ambrosch-Draxl, Phys. Rev. B **59**, 411 (1999).

[23] N. E. Brener, J. M. Tyler, J. Callaway, D. Bagayoko, and G. L. Zhao, Phys. Rev. B **61**, 16582 (2000).

[24] J. Kuneš, P. Novák, P. M. Oppeneer, C. König, M. Fraune, U. Rüdiger, G. Güntherodt, and C. Ambrosch-Draxl, Phys. Rev. B **65**, 165105 (2002).

[25] H. Brändle, D. Weller, J. C. Scott, J. Sticht, P. M. Oppeneer, and G. Güntherodt, Int. J. Mod. Phys. B **7**, 345 (1993).

[26] H. Rathgen, M. I. Katsnelson, O. Eriksson, and G. Zwicknagl, Phys. Rev. B **72**, 014451 (2005).

[27] R. D. Averitt, A. I. Lobad, C. Kwon, S. A. Trugman, V. K. Thorsmølle, and A. J. Taylor, Phys. Rev. Lett. **87**, 017401 (2001).

[28] R. Yamamoto, Y. Moritomo, and A. Nakamura, Phys. Rev. B **61**, R5062 (2000).

[29] M. K. Stewart, K. B. Chetry, B. Chapler, M. M. Qazilbash, A. A. Schafgans, A. Gupta, T. E. Tiwald, and D. N. Basov, Phys. Rev. B **79**, 144414 (2009).

[30] Y. H. Ren, M. Ebrahim, H. B. Zhao, G. Lüpke, Z. A. Xu, V. Adyam, and Q. Li, Phys. Rev. B **78**, 014408 (2008).

[31] G. Müller, J. Walowski, M. Djordjevic, G.-X. Miao, A. Gupta, A. V. Ramos, K. Gehrke, V. Moshnyaga, K. Samwer, J. Schmalhorst, A. Thomas, A. Hütten, G. Reiss, J. S. Moodera, and M. Münzenberg, Nat. Mater. **8**, 56 (2009).

[32] Z. J. Yang and M. R. Scheinfein, J. Appl. Phys. **74**, 6810 (1993).

[33] Š. Višňovský, Czech. J. Phys. B **34**, 969 (1984).

[34] J. M. Florczak and E. D. Dahlberg, Phys. Rev. B **44**, 9338 (1991).